

Harnessing vibrational resonance to identify and enhance input signals

P. Ashokkumar,^{1,2, a)} R. Kabilan,^{1, b)} M. Sathish Aravindh,^{2, c)} A. Venkatesan,^{1, d)} and M. Lakshmanan^{2, e)}

¹⁾*PG & Research Department of Physics, Nehru Memorial College (Autonomous), Affiliated to Bharathidasan University, Puthanampatti, Tiruchirappalli - 621 007, India.*

²⁾*Department of Nonlinear Dynamics, School of Physics, Bharathidasan University, Tiruchirappalli - 620 024, India.*

We report the occurrence of vibrational resonance (VR) and the underlying mechanism in a simple piecewise linear electronic circuit, namely the Murali-Lakshmanan-Chua (MLC) circuit, driven by an additional biharmonic signal with widely different frequency. When the amplitude of the high-frequency force is tuned, the resultant vibrational resonance is used to detect the low-frequency signal and also to enhance it into a high-frequency signal. Further, we also show that even when the low-frequency signal is changed from sine wave to square and sawtooth waves, vibrational resonance can be used to detect and enhance them into high-frequency signals. These behaviors, confirmed by experimental results, are illustrated with appropriate analytical and numerical solutions of the corresponding circuit equations describing the system. Finally, we also verify the signal detection in the above circuit even with the addition of noise.

Vibrational resonance is a phenomenon that occurs in typical nonlinear systems where a weak low-frequency signal can be strengthened by a high-frequency signal, according to Landa and McClintock. The mechanism of vibrational resonance is the interaction of the two-frequency signals, which helps the quality of the weak low-frequency signal in the output to be enhanced. In this paper, we succeed in showing the enhancement of the quality of the weak low-frequency signal in the output of a driven Murali-Lakshmanan-Chua circuit by adding a high-frequency signal. The results of our investigation show that the different signals, namely sine, square, and sawtooth waves, can be identified and enhanced through vibrational resonance. These behaviors are confirmed by numerical and experimental studies. Also, we have verified the tolerance of the nature of the output against noise.

and experimental reports of this VR effect in bistable electrical oscillators have been made^{7,8}. Its potential applications are now being widely researched in a broad range of systems such as bistable systems^{2,9}, multistable systems^{3,5,10}, excitable systems¹¹, delayed dynamical systems^{12,13}, coupled neural oscillators^{4,14-17}, and biological nonlinear systems¹⁸. In particular, the phenomenon of vibrational resonance is used in the implementation of logic gates¹⁹⁻²¹, in the detection of faults in bearings²², to detect a lower level input signal with a higher level amplitude of output²³⁻²⁷, and also in the design of memory devices^{19,28-30}.

Recently, two of the present authors and Venkatesh have found that the quasiperiodically driven Murali-Lakshmanan-Chua (QPDMLC) system mimics dynamic logic gates and basic R-S flip-flops^{31,32}. In their study, they used two square waves to mimic the different logic behaviors and memory functions. In the recent literature, a few authors have applied vibrational resonance to investigate signal detection and enhancement. It was shown that a driven nanoelectromechanical weak signal that has had its nonlinear resonance strengthened makes up a single-stable system³³. A high-frequency character signal has been formulated and fault detected using vibrational resonance in a stable state³⁴. Aperiodic and periodic weak signals were detected numerically using vibrational resonance^{23,35,36}. Generally, for vibrational resonance, one will use two forces, both of which are uniform². Naturally, a question arises here as to whether one can change the low-frequency signal from sinusoidal to square or sawtooth force and fix the second force to be just sinusoidal and then predict the low-frequency signal (sine, square, and sawtooth) without altering the parameters or the second external force. We address this issue in this paper using a simple nonlinear circuit, both numerically and experimentally.

A basic nonlinear circuit, namely Murali-Lakshmanan-Chua (MLC) circuit, characterized by its rich content and simplicity, has garnered significant attention in the literature regarding nonautonomous chaotic circuits, see Fig.1(a)^{9,37}. It consists of an inductor, a capacitor, a resistor, and Chua's diode. As inductors are discrete in nature, they impose limitations on the ability to implement MLC circuits as integrated circuits (ICs). Conversely, in electronic circuits, the inductor is a less preferable circuit element. This is the result of a mul-

I. INTRODUCTION

In a nonlinear system, the phenomenon of vibrational resonance (VR) takes place when weak periodic signals are amplified by the high periodic force present therein¹. Due to the significance of their potential applications, high-frequency signal and VR phenomenon have been studied in different nonlinear dynamical systems². There are many branches of science that use two-frequency signals³, including brain dynamics⁴, where bursting neurons may exhibit two different scales, and communication technology, where low-frequency signals are usually modulated by high-frequency signals^{1,5}, which encode the data⁶.

In particular, this phenomenon was first reported by Landa and McClintock¹ in a bistable system driven by a biharmonic force with widely different frequencies. Both computational

^{a)}Electronic mail: ak3phys@gmail.com

^{b)}Electronic mail: kabilanrajagopal82@gmail.com

^{c)}Electronic mail: sathisharavindh@gmail.com

^{d)}Electronic mail: av.phys@gmail.com

^{e)}Electronic mail: lakshman.cnld@gmail.com

titude of factors. For instance, inductors are comparatively less conventional than the remaining circuit components and necessitate individual preparation for the majority of applications. Furthermore, their spatial dimensions are more sizable, rendering them unsuitable for VLSI implementation unless the inductance is relatively negligible. Numerous inductorless implementations of chaotic circuits have been suggested as a consequence of this^{38–44}.

Compared to neural networks, state-controlled cellular neural networks (SC-CNNs) are a paradigm for parallel computation⁴⁵. A typical SC-CNN is composed of a vast quantity of identical, interconnected dynamical systems known as cells. The fundamental representation of these cells, or nodes is usually expressed in terms of coupled nonlinear ordinary differential equations. Narrow-band processing units are frequently denoted by the terms neurons or cells. Typically two CNN cells are utilized in the construction of the above MLC circuit, see Fig.1(b), in addition to external forces such as biasing, noise, and sinusoidal force^{40,41,43}. Utilizing such an SC-CNN based MLC circuit to extend the analysis to the coupled system is extremely useful.

The theme of this paper is to study the underlying dynamical phenomenon of vibrational resonance in the presence of two different forces in a piecewise linear non-autonomous system, and in particular in the Murali-Lakshmanan-Chua (MLC) system using the State Controlled - Cellular Neural Networks (SC-CNNs). We have also carried out appropriate numerical studies on the SC-CNN MLC circuit when additional low and high-frequency signals are present. Also, in the present study, we point out that, in contrast to the earlier investigation in Ref.¹⁹, for the appropriate choice of system parameters, one can identify VR with a maximal response over a wide range of high-frequency amplitudes, which will enable assured applications in signal detection and enhancement. Particularly the low input signals are in the form of sinusoidal, square wave, or sawtooth types. The obtained numerical results for the detection and enhancement of low-frequency signals are compared and confirmed with the corresponding experimental results. Finally, we demonstrate a robust principle to detect the low-intensity signal via vibrational resonance even in the presence of additional Gaussian white noise.

The structure of this paper is as follows: In Section II, we provide an overview of the notion of vibrational resonance in the SC-CNN cell structure of the nonlinear, non-autonomous system. In Sections III, IV and V, we discuss the numerical and experimental realization, respectively, of response amplitude in detecting the low-frequency signal and its enhancement for different input signals. In Section VI, the impact of noise is examined. We conclude by summarizing our findings in Section VII. Also, we discuss the analytical evaluation of the response amplitude in Appendix A.

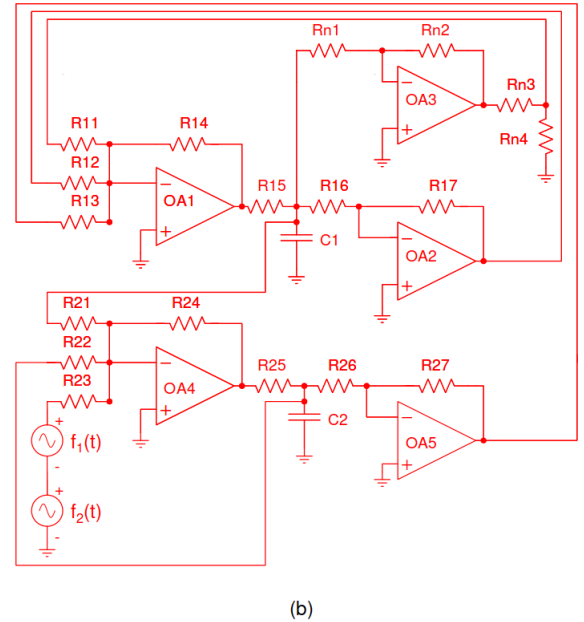
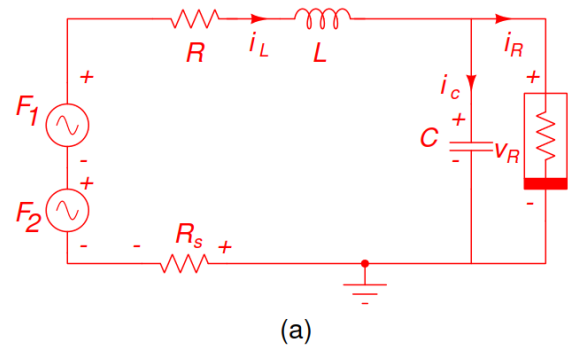


FIG. 1. Panel (a) and (b) shows the schematic diagram for MLC circuit and SC-CNN based MLC circuit.

II. VIBRATIONAL RESONANCE IN STATE CONTROLLED CNN BASED NONLINEAR NON-AUTONOMOUS SYSTEM

The concept of Cellular Neural Network (CNN) was first developed by Chua and Yang in 1988⁴⁵. It is an n-dimensional array of resistors, capacitors, OP-AMPs, and other analog circuit components, but without any inductors. The underlying CNN is built from a large number of interconnected dynamical systems.

CNN is a reasonably basic circuit that may be easily implemented experimentally using appropriate electronic circuit elements. These circuits are powerful tools for the emulation of complex dynamics in nonlinear systems. In this case, the local output and voltage variables of the CNN cells are exchanged with one another. This generalization uses the analog components of CNN and it is known as the State Controlled - CNN (SC-CNN). Many chaotic circuits designed and implemented in terms of SC-CNN have been documented in the literature^{40,42,43,46–49}. The significant advantages of these CNN circuits are fourfold, that is (1) they have no inductors, (2) their only circuitry is RC based, (3) they are parallelly

connected, and (4) they consume less power. Thus the SC-CNN circuits are realized with less number of hardware and are easily implemented in VLSI design⁵⁰. The present study illustrates that, after adding an additional sine wave signal to this circuit, the resultant output exhibits similar and inverted enhanced sine wave signals. Further, this phenomenon is also illustrated for as other signals such as square wave and saw-tooth wave.

The single forced SC-CNN MLC circuit has been well studied at the numerical, experimental, and analytical levels in ref.⁴⁰. The standard MLC circuit [see Fig.1(a)] consists of a nonlinear resistor that has the three-segment piecewise characteristics of Chua's diode, a linear resistor, a linear inductor, and a linear capacitor with a sinusoidal voltage source^{9,37}.

It is a well-established fact^{9,37} that the normalized form of the MLC circuit equation with additional sinusoidal force connected in series (Fig.1(a)) can be written as

$$\begin{aligned} \dot{x} &= y - h(x), \\ \dot{y} &= -\beta(1 + \nu)y - \beta x + f_1 \sin(\omega_1 t) + f_2 \sin(\omega_2 t), \end{aligned} \quad (1)$$

where the piecewise linear function $h(x)$ is given as

$$h(x) = \begin{cases} bx + (a - b), & x > 1, \\ ax, & |x| \leq 1, \\ bx - (a - b), & x < -1. \end{cases} \quad (2)$$

The relationship between the various circuit variables and circuit parameters and the above dynamical variables and parameters can be obtained from Refs.^{9,37,51}. Earlier studies on the dimensionless version of the circuit with a single external periodic force for the chosen parametric values $a = -1.02$, $b = -0.55$, $\gamma = 0.015$, $\beta = 1.0$ and $\omega_1 = 0.75$ is readily available in the literature. In these studies, the quantity f_1 , which is the amplitude the first periodic force, was varied to identify different bifurcation structures. It has been shown that this dynamical system exhibits chaos via different routes, including the period-doubling route, intermittency route, and strange non-chaotic attractor (SNA) route, among others^{9,51}.

The dynamic model of the circuit (Fig.1(b)) of two generalized CNN cells is in accordance with the following coupled state equations,

$$\begin{aligned} \dot{x}_1 &= -x_1 + a_{11}y_1 + a_{12}y_2 + \sum_{k=1}^2 s_{1k}x_k + i_1, \\ \dot{x}_2 &= -x_2 + a_{21}y_1 + a_{22}y_2 + \sum_{k=1}^2 s_{2k}x_k + i_2, \end{aligned} \quad (3)$$

where x_1 and x_2 are state variables, and y_1 and y_2 are the corresponding outputs. The MLC circuit equation defined by Eq.(1) can be derived from Eq.(3), by assuming $x = x_1$, $y = x_2$, $a_1 = b - a$, $a_{12} = a_{21} = a_2 = 0$, $s_{11} = 1 - b$, $s_{12} = 1$, $s_{21} = -\beta$, $s_{22} = 1 - \beta(1 + \nu)$, $i_1 = 0$ and $i_2 = f_1 \sin(\omega_1 t) + f_2 \sin(\omega_2 t)$.

Consequently, from Eq.(3), the SC-CNN based MLC circuit model (Fig.1(b)) is organized as below :

$$\begin{aligned} \dot{x}_1 &= -x_1 + a_{11}y_1 + s_{11}x_1 + s_{12}x_2, \\ \dot{x}_2 &= -x_2 + s_{21}x_1 + s_{22}x_2 + f_1 \sin(\omega_1 t) + f_2 \sin(\omega_2 t), \end{aligned} \quad (4)$$

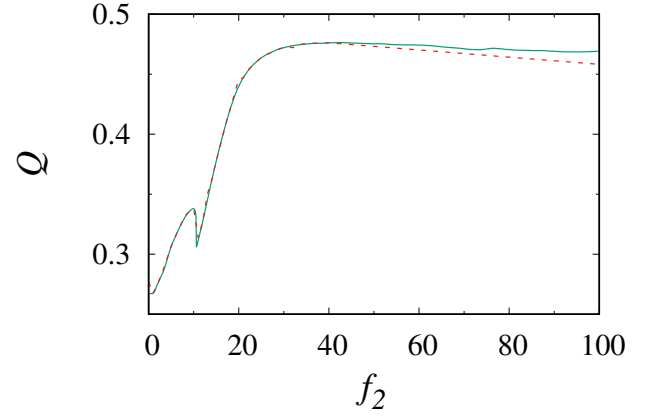


FIG. 2. The dependence of response amplitude Q with f_2 . The solid line and dashed line represent the numerical and analytical response amplitudes, respectively, for a fixed set of values of parameters with $\omega_1 = 0.75$, $\omega_2 = 3.5$, and the forcing parameter $f_1 = 0.25$.

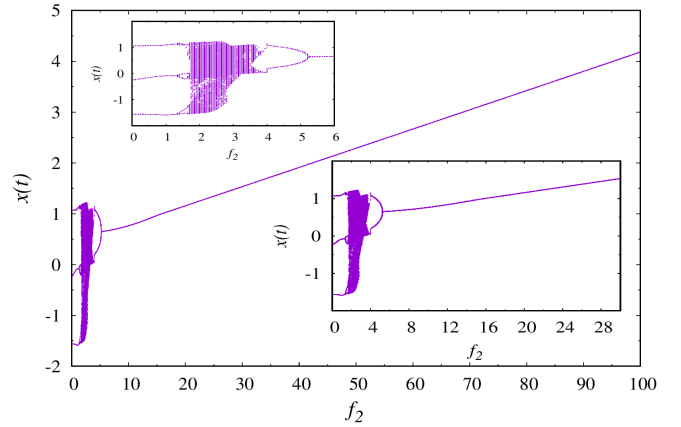


FIG. 3. Bifurcation diagram of f_2 vs $x(t)$. The sub-figure shows the enlarged version of external force f_2 for a fixed set of values of parameters with $\omega_1 = 0.75$, $\omega_2 = 3.5$, and the forcing parameter $f_1 = 0.25$.

where y_1 is the piecewise linear function,

$$y_1 = f(x_1) = 0.5(|x_1 + 1| - |x_1 - 1|). \quad (5)$$

Here, the external forces $f_1 \sin(\omega_1 t)$ and $f_2 \sin(\omega_2 t)$ correspond to low and high level frequencies, respectively, where the amplitude $f_1 = 0.25$ is fixed while f_2 is varied. Further, the following are typically the rescaled parameter values: $a_1 = 0.47$; $s_{11} = 1.550$; $s_{12} = 1.0$; $s_{21} = -1.0$; $s_{22} = -0.015$; $\omega_1 = 0.75$; $\omega_2 = 3.5$; and $f_1 = 0.25$. For suitable choices of the control parameter value f_2 , the system exhibits a rich variety of dynamics. In the present paper, we investigate the effect of vibrational resonance, detect the existence of a low input frequency signal in the corresponding response, and also obtain the enhancement of it to a high-frequency signal in this circuit.

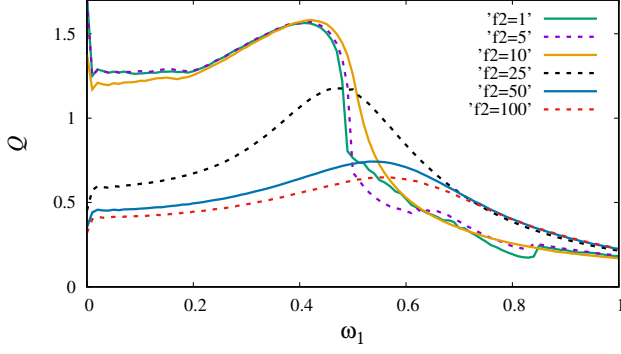


FIG. 4. The dependence of response amplitude Q with ω_1 for different values of f_2 . Different colors indicate different values of the second forcing parameter f_2 . The remaining parameters are fixed with $\omega_2 = 3.5$, and the first forcing parameter $f_1 = 0.25$.

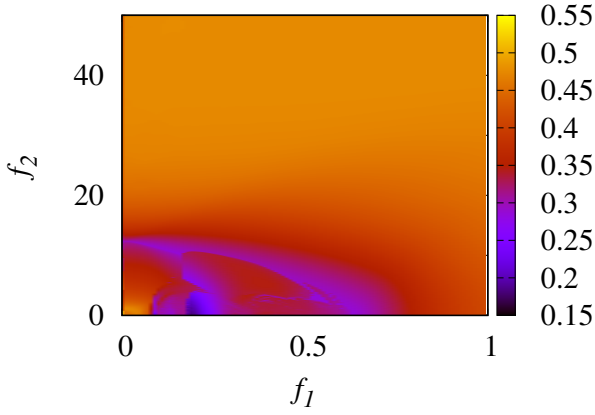


FIG. 5. The maximum response amplitude Q depicted in a two-parameter phase diagram for the amplitude of the first force f_1 vs second force f_2 for fixed parameters $\omega_1 = 0.75$ and $\omega_2 = 3.5$.

III. ANALYTICAL AND NUMERICAL EVALUATION OF RESPONSE AMPLITUDE

The analytical expression for the response function can be explicitly obtained using the exact solution of the dynamical equation of the MLC circuit equation (1)-(2) in the three different piecewise regions of the Chua's diode. This is carried out in Appendix A. Consequently, we obtain

$$Q_{ana} = \frac{\sqrt{(\sum Q_s^{0,\pm})^2 + (\sum Q_c^{0,\pm})^2}}{f_1}, \quad (6)$$

where $Q_s^{0,\pm}$, $Q_c^{0,\pm}$ are given in Eqs.(A14) and (A15) in Appendix A. To obtain the corresponding response amplitude from numerical analysis, we proceed as follows.

After solving numerically Eq.(4) and using the results in the following expression for the response function, after discard-

ing the transients, we obtain¹

$$Q_{num} = \frac{\sqrt{Q_s^2 + Q_c^2}}{f_1}, \quad (7)$$

over a range of values of the forcing strength of high-frequency driving force (f_2). Here the values of the quantities Q_s and Q_c are computed from the Fourier spectrum of the time series of the output signal $x(t)$ as

$$Q_c = \frac{2}{nT} \int_0^{nT} x(t) \cos(\omega_1 t) dt, \\ Q_s = \frac{2}{nT} \int_0^{nT} x(t) \sin(\omega_1 t) dt, \quad (8)$$

where n is an integer. The response curves of Q versus selected parameters for a range of system parameters are numerically calculated. The system (4) is numerically integrated with Runge-Kutta fourth order algorithm with step size $\Delta t = 0.01$.

The analytically and numerically calculated response amplitudes from Eq.(6) and Eq.(7) are shown in Fig.2. The solid and dashed lines represent the numerical and analytical response amplitudes, respectively. To obtain these curves, we fix the system parameter values as $\omega_1 = 0.75$, $\omega_2 = 3.5$ and $f_1 = 0.25$. The remaining parameter, f_2 , is selected in such a way that it promotes the emergence of VR. It is obvious from Fig.2 that as the high-frequency force f_2 increases, the response amplitude slowly increases and reaches a first maximum value when $f_2 = 10.0$. After this, there is a sudden drop in the response amplitude, and then it again increases until the response amplitude reaches its maximum value around $f_2 = 25.0$. Any further increase in f_2 does not lead to any notable change in the value of Q . It is also instructive to look at the nature of the corresponding dynamics, which can be identified from the structure of the associated bifurcation diagram. Fig.3 exhibits the bifurcation diagram for different values of the high forcing parameter f_2 . Initially, for low f_2 the system exhibits period-3 oscillations ($f_2 \in [0, 1.30]$); on further increase in f_2 , the system exhibits period doubling phenomenon in the range of $f_2 \in [1.30, 1.65]$ and exhibits chaotic behavior for $f_2 \in [1.65, 3.66]$. After this beyond $f_2 = 3.66$ the system shows reverse period doubling phenomenon for the range of $f_2 \in [3.66, 5.3]$. After the forcing parameter f_2 reaches the value $f_2 = 5.3$, the system exhibits period-1 oscillations. Further, by increasing the forcing parameter $f_2 > 5.3$, the system continuously exhibits period-1 oscillations behavior. Also, with the increase of f_2 , the response Q reaches a maximum value when $f_2 = 10.0$, after which one observes a sudden drop in the response amplitude (see Fig.2), and then it again increases as f_2 increases until f_2 reaches the value around $f_2 = 25.0$ beyond which saturation arises. Here again the system exhibits limit cycle oscillations in this range of $f_2 \in [5.3, 100]$ ^{9,37}. The sub-figure Figs.3 show the enlarged version as a function of the external forcing parameter f_2 , $f_2 \in [0, 30]$.

Further in Fig.4, we present the response amplitude against the first forcing frequency ω_1 for different values of the forc-

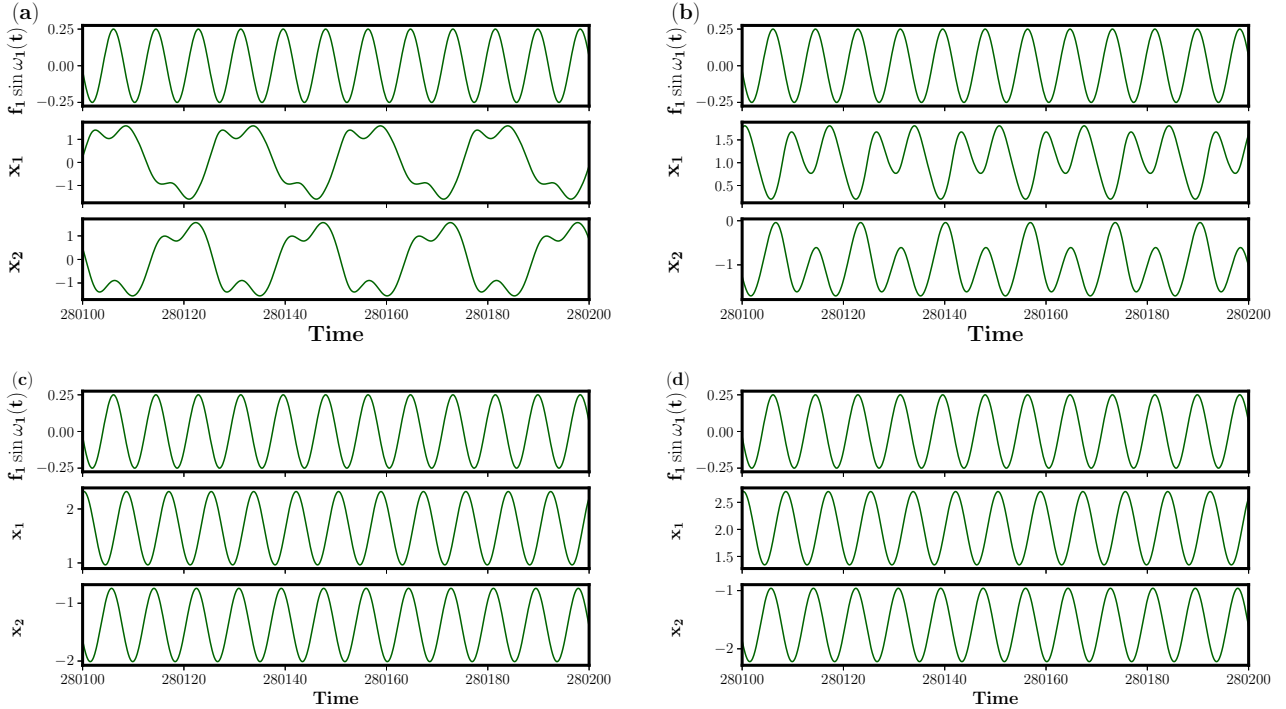


FIG. 6. Realization of the signal detection in the numerical simulation : Panels (a)-(d) correspond to different values of f_2 , $f_2 = 1.0, 5.0, 15.0$ and 25.0 , respectively. Every panel is having three sub-figures, namely the low amplitude signal f_1 , and the resultant outputs x_1 and x_2 .

ing parameter f_2 . Different values of f_2 are indicated by different colors in Fig.4. Initially, at a low-frequency of f_2 , we obtain a high response at a low value of ω_1 . On increasing the value of f_2 , the maximum of the response amplitude shifts to larger value of ω_1 . For all the values of f_2 , the response curves exhibit a saturation at higher values of ω_1 .

Fig.5 is a 3-dimensional plot that depicts the numerically computed response as a function of the first forcing strength f_1 of low-frequency signal and the second forcing strength f_2 of high-frequency. It is clearly demonstrated in Fig.5 that the response amplitude ‘ Q ’ is constant for the higher value of the second forcing strength f_2 . Increasing the low-frequency signal $f_1 \in [0, 1]$, the response amplitude attains the maximum value for a low value of the second forcing signal f_2 . In Fig.6 every panel indicates the three signals, namely the low input signal f_1 and the outputs x_1 and x_2 . Let us consider first the low input signal for $f_1 = 0.25$ and the second forcing signal $f_2 = 1.0$. The corresponding outputs x_1 and x_2 are shown in Fig.6(a). The two outputs x_1 and x_2 randomly oscillate and do not match with the low input signal f_1 . On further increasing the f_2 value to $f_2 = 5.0$, the outputs x_1 and x_2 slowly approach the actual input behavior [see Fig.6(b)]. At $f_2 = 15.0$, we find the outputs x_1 and x_2 approach exactly the sinusoidal behavior where the output x_2 matches with the low input signal f_1 , and the other output x_1 inversely matches it. Also, the output signals get enhanced in comparison with the input signal f_1 [see Fig.6(c)]. Then, on further increase in the f_2 value to $f_2 = 25.0$ and beyond, that is in the range $f_2 \in [25, 200]$, the outputs x_1 and x_2 accurately predict the frequency of the input

signal f_1 continuously in the form of inverse and similar signals, respectively [see Fig.6(d)]. Also, the response outputs are enhanced in comparison with the low input signal f_1 .

IV. EXPERIMENTAL REALIZATION

Using experimental realization, in the following, we verify the results obtained by numerical simulation discussed in the earlier sections. Now we consider the biharmonic forced SC-CNN based Murali-Lakshmanan-Chua circuit given in Fig.1(b) with the circuit cell components $R_{11} = 207 K\Omega$, $R_{12} = 66 K\Omega$, $R_{13} = 100 K\Omega$, $R_{14} = 100 K\Omega$, $R_{15} = 1 K\Omega$, $R_{16} = 100 K\Omega$, $R_{17} = 100 K\Omega$, $R_{n1} = 220 K\Omega$, $R_{n2} = 3 M\Omega$, $R_{n3} = 180 K\Omega$, $R_{n4} = 16 K\Omega$, $R_{21} = 100 K\Omega$, $R_{22} = 6666.6 K\Omega$, $R_{23} = 100 K\Omega$, $R_{24} = 100 K\Omega$, $R_{25} = 1 K\Omega$, $R_{26} = 100 K\Omega$, $R_{27} = 100 K\Omega$, $R_{31} - R_{38} = 10 K\Omega$, $C_1 = 10 nF$, $C_2 = 10 nF$ and active element $IC741$ type voltage OP-AMPs with $\pm 12 V$ supply voltages. Experimental results were obtained using Agilent function generators (33220A) and Agilent digital storage oscilloscopes ($DSO 7014B$). The changes in the dynamics of the circuit under the effect of input streams are obtained by measuring the voltages v_1 and v_2 across the capacitors C_1 and C_2 , respectively. Further, we vary the second forcing parameter f_2 from 100 mV to 1 V. In this case, Fig.7(a) shows the low input signal f_1 and two output signals v_1 and v_2 . The first input f_1 is fixed as 100 mV and the second input f_2 is also given the value 100 mV. The corresponding outputs of the system signals do not predict the low-frequency input sig-

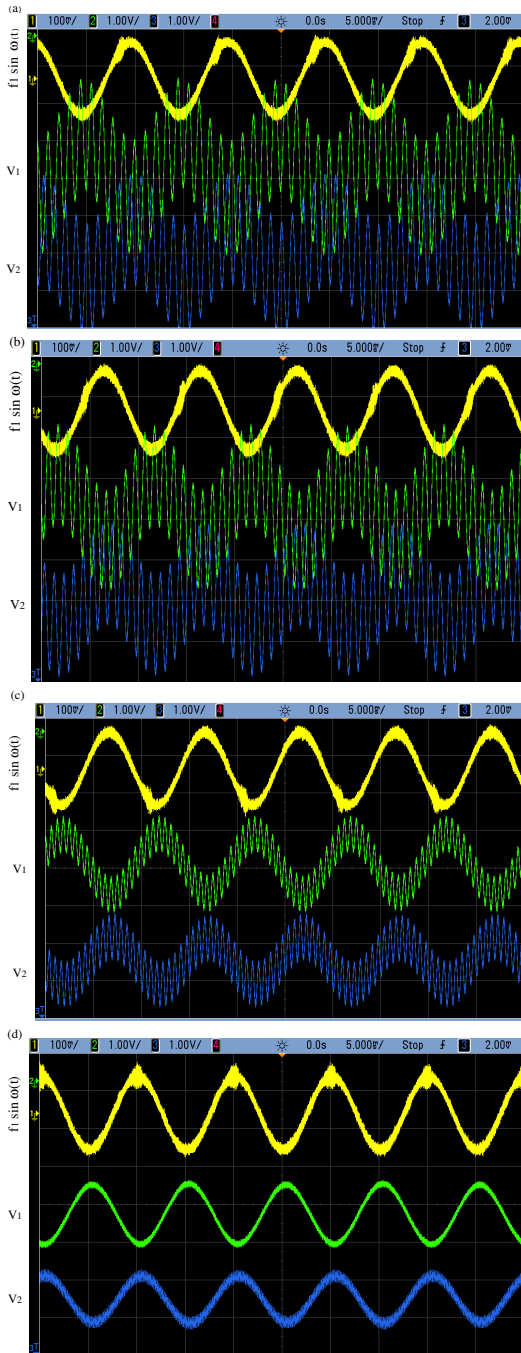


FIG. 7. Realization of the signal detection in experimental SC-CNN based MLC electronic circuit : Panels (a)-(d) correspond to different values of f_2 , $f_2 = 100$ mV, 300 mV, 700 mV , and 1.0 V, respectively. Every panel is having three sub-figures namely the low amplitude signal f_1 , and the experimental outputs v_1 and v_2 .

signals f_1 (fig.7(a)). As f_2 is increased to 300 mV (fig.7(b)) the lower input is not observed in the output signal. On further increase to the value $f_2 = 700$ mV (see fig.7c), the output signals are able to replicate the low input signals f_1 . Even further increase of f_2 to $f_2 = 1.0$ V (see Fig.7d), the lower input signal is predicted from the output signal v_2 (and its inverse from

v_1) and also the amplitude gets enhanced from 100 mV to 1 V (see the panel at the top of every figure in Fig.7). On further increase in the value of f_2 , the output signals are able to detect the lower input signal continuously.

V. ANALYZING THE BEHAVIOR OF DIFFERENT LOW-FREQUENCY INPUT SIGNALS f_1

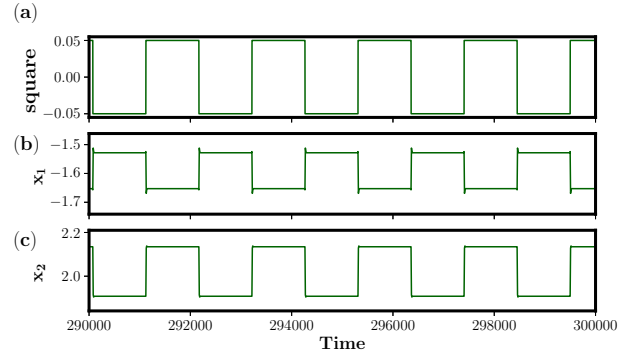


FIG. 8. Realization of the signal detection in the numerical simulation: Panels (a)-(c) correspond to low amplitude square wave, and the resultant outputs x_1 and x_2 for a fixed value of $f_2 = 25.0$.

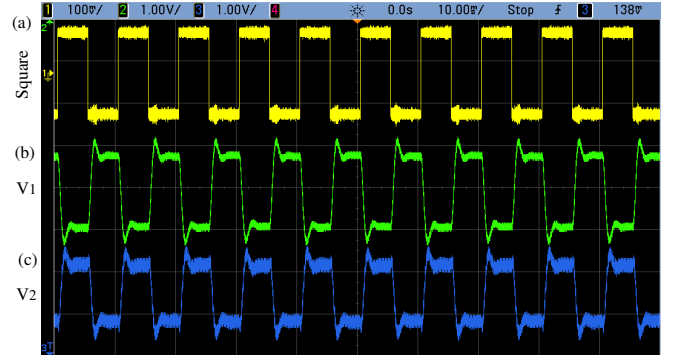


FIG. 9. Realization of the signal detection in the experimental realization: Panels (a)-(c) correspond to low input of square wave, and the resultant experimental outputs v_1 and v_2 .

Next, we pose an interesting question: is it possible to detect other types of wave profiles like square, sawtooth, etc. waves which are different from sinusoidal ones? The answer is yes if one changes the low-frequency signal from a sine to a square or sawtooth wave, as discussed below. For this purpose, we fix the high-frequency signal f_2 as a sine wave and change the low-frequency signal f_1 from a sine wave to a square or sawtooth wave. Figs.8 and 9 show the corresponding numerical and experimental outputs of the square wave. Also, Figs.10 and 11 show the corresponding numerical and experimental outputs of the sawtooth wave. In particular, Figs.8 and 10 indicate the three panels (a)-(c), namely the low input signal square/sawtooth wave and the corresponding numerical outputs x_1 and x_2 . The experimental outputs

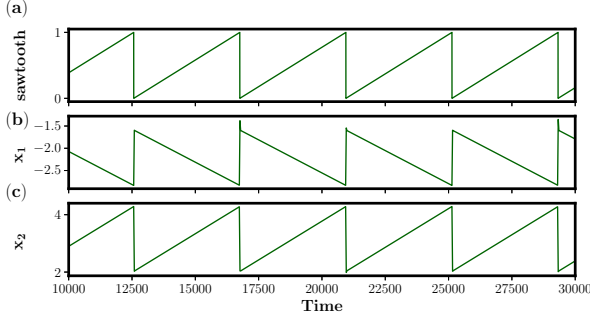


FIG. 10. Realization of the signal detection in the numerical simulation: Panels (a)-(c) correspond to low amplitude sawtooth wave, and the resultant outputs x_1 and x_2 for a fixed value of $f_2 = 25.0$.

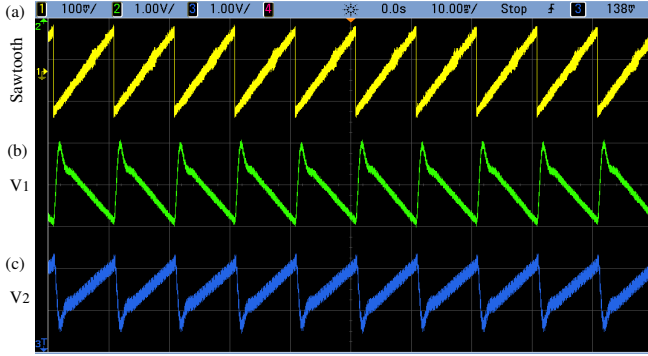


FIG. 11. Realization of the signal detection in the experimental realization: Panels (a)-(c) correspond to low input of sawtooth wave, and the resultant experimental outputs v_1 and v_2 .

Figs.9 and 11 indicate the three panels (a) – (c), namely the low input signal square/sawtooth wave and the corresponding resultant outputs v_1 and v_2 . The corresponding numerical and experimental outputs x_1/v_1 and x_2/v_2 are shown in Figs.8/10 and 9/11. These outputs x_1/v_1 and x_2/v_2 approach exactly the square and sawtooth waveforms and accurately predict the frequency of the square and sawtooth wave input signals continuously in the form of inverse and similar signals, respectively [see Figs.8/10 and 9/11]. Also, the response outputs are enhanced in comparison with the low input signal. Thus, we confirm using different input signals like square/sawtooth wave signals that we are able to detect and enhance the output signals through numerical and experimental realizations.

VI. EFFECT OF NOISE

At this point, a question that may naturally arise is whether or not the system exhibits the same kind of structure after the inclusion of additional noise. Now we reexpress Eq.(4) after including the Gaussian white noise as below,

$$\begin{aligned} \dot{x}_1 &= -x_1 + a_{11}y_1 + s_{11}x_1 + s_{12}x_2, \\ \dot{x}_2 &= -x_2 + s_{21}x_1 + s_{22}x_2 + f_1 \sin(\omega_1 t) + f_2 \sin(\omega_2 t) + D\xi(t). \end{aligned} \quad (9)$$

In the above equation Eq.(9) $\xi(t)$ represents the Gaussian

white noise and D is its strength. We fix the forcing parameters as $f_1 = 0.25$ and $f_2 = 25.0$ and vary the noise strength D . The numerically calculated time series outputs from Eq.(9) is shown in Fig.12. Every panel in Fig.12 contains four figures, which correspond to the following: the low input signal f_1 , noise D , and the outputs x_1 and x_2 . Let us consider the low input signal with $f_1 = 0.25$, a second forcing signal $f_2 = 25.0$, and noise $D = 0.0$. Fig.12(a) depicts the corresponding outputs x_1 and x_2 . In the form of inverse and similar signals, the two outputs, x_1 and x_2 , continuously predict the frequency of the input signal, f_1 . When the value of D is increased further to $D = 0.1$, the outputs x_1 and x_2 continue to take the form of the input behavior [see Fig.12(b)]. As the D value is increased further to $D = 0.5$, the outputs x_1 and x_2 gradually lose their actual input behavior [see Fig.12(c)]. The output signals x_1 and x_2 then randomly oscillate and do not match with the low input signal f_1 as the value of D increases to $D = 1.0$ and beyond [see Fig.12(d)].

Next, we include the noise in the experimental SC-CNN based MLC circuit (Fig.1(b)) in series with signal f_1 and f_2 . By measuring the voltages v_1 and v_2 across the capacitors C_1 and C_2 , respectively, the realization of experimental output and changes in the dynamics of the circuit under the effect of noise are obtained. In our experimental investigation, we are using an *Agilent* function generator (33220A) and it has a noise signal option to generate the noise signal. The noise bandwidth of this function generator has been fixed at 9 MHz, which is typical. In our study, we vary the amplitude $D\xi(t)$ of the noise signal (see Fig.13(a-d) second channel). Further, we fix the forcing parameters as $f_1 = 100$ mV and $f_2 = 1$ V and vary the noise parameter D from 0 V to 2.6 V. Fig.13(a) depicts the low input signal f_1 , the noise input signal $D = 0.0$ V, and two output signals v_1 and v_2 in this case. When no noise is present, $D = 0.0$ V, the first and second inputs, f_1 and f_2 , are set to 100 mV and 1 V, respectively. The frequencies of the corresponding outputs v_1 and v_2 exactly predict that of the lower input signal f_1 (as shown in Fig.13(a)). As D is increased to 500 mV, the lower input signal is continued to be observed in the output signals (Fig.13(b)). As the value D is increased further to $D = 1.5$ V(see Fig.13(c)), the output signals gradually miss matching the input signals. When increasing the strength D to $D = 2.6$ V (see Fig.13(d)), the system output signals are too weak to predict the low-frequency input signal. On further increasing the strength of the noise signal, one finds that the system no longer has the ability to mimic the input signal.

Fig.14 shows the probability of detecting or imitating the input signal after taking the noise strength (D) into account. The area to detect/mimic the weak input signal is indicated by the red dots. With strength D , we determine the probability $P(\text{signal})$ of receiving the same input structure for various noise intensities. $P(\text{signal})$, in its simplest form, represents the proportion of total successful runs to total runs. $P(\text{logic})$ is given the value "1" if the system displays the intended input signal in response output; otherwise, it is handled as "0". A sampling of 2000 runs of the given input set is used to calculate $P(\text{signal})$ for the system (9), and this process is repeated 1000 times. We use a low D value for the output signal in

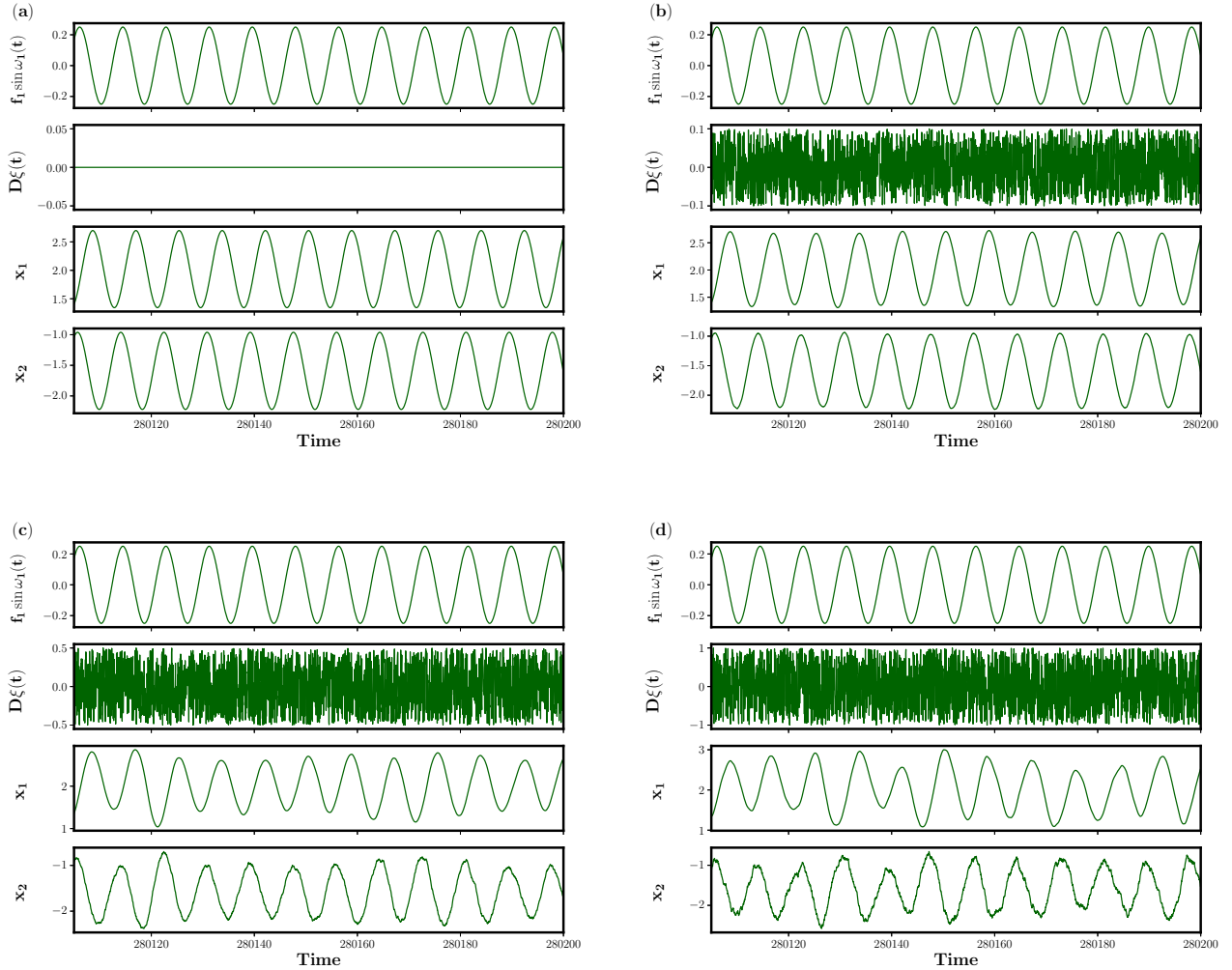


FIG. 12. Realization of the signal detection in numerical simulation: Panels (a)-(d) corresponds to different values of D . Panel (a) represents $D = 0.0$, panel (b) represents $D = 0.1$, panel (c) represents $D = 0.5$ and panel (d) represents $D = 1.0$ with fixed forcing parameter $f_1 = 0.25$ and $f_2 = 25.0$. Every panel is having four subfigures namely low amplitude $f_1 \sin \omega_1 t$, Gaussian white noise $D\xi(t)$, and the resultant outputs x_1 and x_2 .

order to recognize or mimic the low input signal f_1 . The noise progressively ceases matching the weak input signal f_1 as the noise level increases. Hence, even in the presence of noise coming from electronic components or any other external variables, the system's ability to recognize or replicate the low input signal is conclusively proven.

VII. CONCLUSIONS

In summary, we have demonstrated the existence of vibrational resonance in a nonlinear, nonautonomous SC-CNN-based MLC circuit. We have explained how the amplitude of the driving signal interacts with the state of the system through analytical, numerical and experimental studies. Particularly, we used two different forces with widely varying frequencies

that contribute to generating vibrational resonance in the SC-CNN based MLC circuit. These forces work together to extend the region of resonance at specific system parameter values. Apart from this, we have also demonstrated the idea of detecting low input signals and obtaining enhanced output signals, which is one of the significant roles played by vibrational resonance in nonlinear systems. Besides these, we have also detected different low-input signals, such as square and sawtooth waves, in the same circuit without altering the system parameter values. We have also confirmed the robustness of detecting and enhancing the signal even after adding external Gaussian white noise.

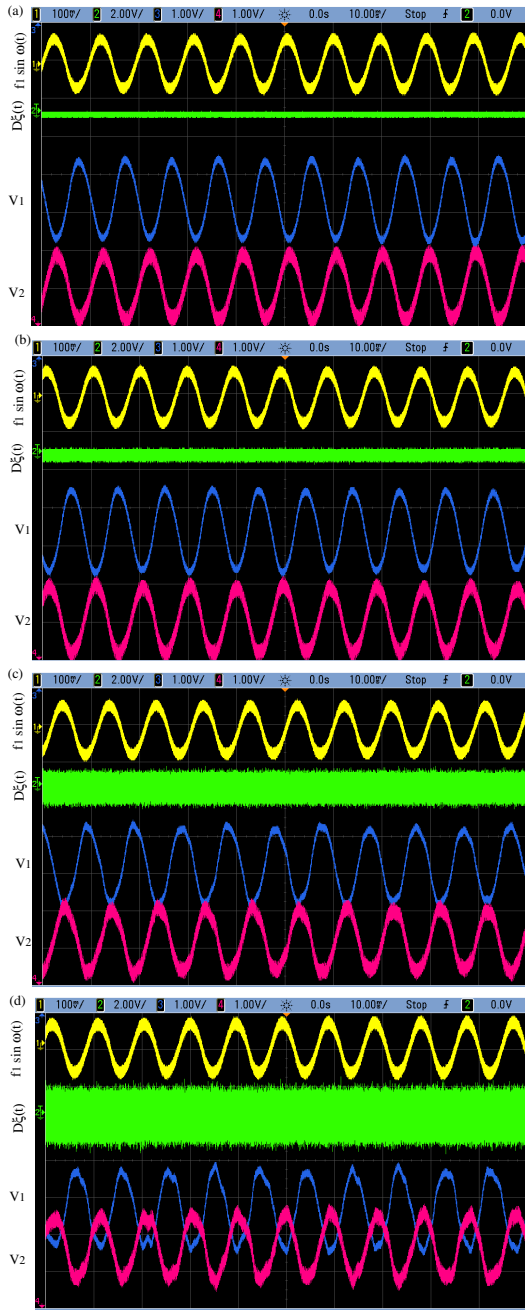


FIG. 13. Realization of the signal detection in experimental electronic circuits: Panels (a)-(d) correspond to different values of D with fixed $f_1 = 100$ mV and $f_2 = 1$ V. Panel (a) represents $D = 0$ V, panel (b) represents $D = 500$ mV, panel (c) represents $D = 1.5$ V, and panel (d) represents $D = 2.6$ V. Every panel is having four subfigures namely low amplitude $f_1 \sin(\omega_1 t)$, Gaussian white noise $D\xi(t)$, and the experimental outputs v_1 and v_2 .

ACKNOWLEDGMENT

The authors wish to thank Dr. P. R. Venkatesh for providing support in the analytical calculations. A.V. thanks the DST-FIST for funding research projects via Grant No. SR/FST/College-2018-372 (C). M.L. wishes to acknowledge

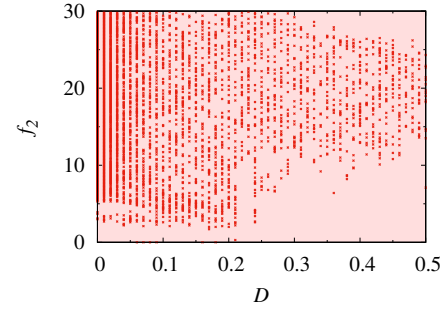


FIG. 14. The maximum response amplitude Q depicted in a two-parameter phase diagram for noise strength D vs second force f_2 for fixed parameters $f_1 = 0.25$, $\omega_1 = 0.75$ and $\omega_2 = 3.5$.

the DST-SERB National Science Chair program for funding under Grant No. NSC/2020/000029 in which PA and MS, respectively, are supported by a Project Associate and a Research Associate.

DATA AVAILABILITY STATEMENT

Data will be made available on request.

Appendix A: Analytical evaluation of the response amplitude

Now the system (1) can be explicitly integrated in terms of elementary functions in each of the three regions D_0 , D_+ and D_- ($|x| \leq 1$, $x > 1$ and $x < -1$) and matched across the boundaries to obtain the full solution as shown below¹⁹.

It is found that in each one of the regions D_0 , D_+ and D_- the driving system (1) can be represented as a single second order inhomogeneous differential equation for the variable $y(t)$,

$$\ddot{y} + (\beta + \beta v + \mu)\dot{y} + (\beta + \mu\beta v + \beta\mu)y = \Delta + \mu f_1 \sin(\omega_1 t) + \omega_1 f_1 \cos(\omega_1 t) + \mu f_2 \sin(\omega_2 t) + \omega_2 f_2 \cos(\omega_2 t), \quad (\text{A1})$$

where

- (i) $\mu = a$, $\Delta = 0$ in region D_0 , and
- (ii) $\mu = b$, $\Delta = \pm\beta(a - b)$ in region D_{\pm} .

The general solution of the system A1 can be written as

$$y(t) = C_{0,\pm}^1 \exp(\alpha_1 t) + C_{0,\pm}^2 \exp(\alpha_2 t) + E_1 + E_{12} \sin(\omega_1 t) + E_{13} \cos(\omega_1 t) + E_{22} \sin(\omega_2 t) + E_{23} \cos(\omega_2 t), \quad (\text{A2})$$

where $C_{0,\pm}^1, C_{0,\pm}^2$ are integration constants in the appropriate regions D_0, D_{\pm} , and

$$\begin{aligned} \alpha_{1,2} &= (-A \pm \sqrt{A^2 - 4B})/2, \\ A &= \beta + \beta v + \mu, \quad B = \beta + \mu\beta v + \beta\mu, \\ E_1 &= 0 \text{ in region } D_0, \quad E_1 = \Delta/B \text{ in region } D_{\pm}, \\ E_{12} &= \frac{[f_1 \omega_1^2 (A - \mu) + \mu f_1 B]}{[A^2 \omega_1^2 + (B - \omega_1^2)^2]}, \quad E_{13} = \frac{f_1 \omega_1 [B - \omega_1^2 - \mu A]}{[A^2 \omega_1^2 + (B - \omega_1^2)^2]}, \\ E_{22} &= \frac{[f_2 \omega_2^2 (A - \mu) + \mu f_2 B]}{[A^2 \omega_2^2 + (B - \omega_2^2)^2]}, \quad E_{23} = \frac{f_2 \omega_2 [B - \omega_2^2 - \mu A]}{[A^2 \omega_2^2 + (B - \omega_2^2)^2]}. \end{aligned}$$

Knowing $y(t)$, we can obtain $x(t)$ from (1) as

$$x(t) = 1/\beta[-\dot{y} - \beta y(1 + \nu) + f_1 \sin(\omega_1)t + f_2 \sin(\omega_2)t]. \quad (\text{A3})$$

Substituting for y and \dot{y} from Eq.(A2), the form of $x(t)$ is found to be

$$x(t) = 1/\beta[-C_{0,\pm}^1(\alpha_1 + \sigma)\exp(\alpha_1 t) - C_{0,\pm}^2(\alpha_2 + \sigma)\exp(\alpha_2 t) + (E_{12}\omega_1 + E_{13}\sigma)\cos(\omega_1 t) + (f_1 - E_{12}\sigma + E_{13}\omega_1)\sin(\omega_1 t) + (E_{22}\omega_2 + E_{23}\sigma)\cos(\omega_2 t) + (f_2 - E_{22}\sigma + E_{23}\omega_2)\sin(\omega_2 t) - E_1\sigma]. \quad (\text{A4})$$

where $\sigma = \beta(1 + \nu)$ and the value of the integration constants, namely $C_{0,\pm}^1$ and $C_{0,\pm}^2$ are obtained by substituting the initial condition at $t = t_0$, $x(t_0) = x_0$ and $y(t_0) = y_0$ in Eqs. (A3) and (A4). On solving further, the explicit form of the integration constants are found as

$$C_{0,\pm}^1 = \exp(-\alpha_1 t_0)/(\alpha_1 - \alpha_2)[- \beta x_0 + [E_{12}\omega_1 + E_{13}(\alpha_2 + 2\sigma)]\cos(\omega_1 t_0) + [f_1 + E_{12}\alpha_2 + E_{13}\omega_1]\sin(\omega_1 t_0) + [E_{22}\omega_2 + E_{23}(\alpha_2 + 2\sigma)]\cos(\omega_2 t_0) + [f_2 + E_{22}\alpha_2 + E_{23}\omega_2]\sin(\omega_2 t_0) - E_1\alpha_2 - y_0(\alpha_2 + \sigma)], \quad (\text{A5})$$

$$C_{0,\pm}^2 = \exp(-\alpha_1 t_0)/(\alpha_2 - \alpha_1)[- \beta x_0 + [E_{12}\omega_1 + E_{13}(\alpha_1 + 2\sigma)]\cos(\omega_1 t_0) + [f_1 + E_{12}\alpha_1 + E_{13}\omega_1]\sin(\omega_1 t_0) + [E_{22}\omega_2 + E_{23}(\alpha_1 + 2\sigma)]\cos(\omega_2 t_0) + [f_2 + E_{22}\alpha_1 + E_{23}\omega_2]\sin(\omega_2 t_0) - E_1\alpha_1 - y_0(\alpha_1 + \sigma)]. \quad (\text{A6})$$

The response of the system is then calculated from the sine and cosine components, Q_s and Q_c , respectively of the output signal $x(t)$.

Using Eq.(A4) the sine and cosine constituents of the output signal are given by

$$Q_s = \frac{2}{nT} \int_0^{nT} x(t) \sin(\omega_1 t) dt, \quad (\text{A7})$$

$$Q_c = \frac{2}{nT} \int_0^{nT} x(t) \cos(\omega_1 t) dt.$$

where $T = 2\pi/\omega_1$ and n is a positive integer. Then, we finally find the dependence on f_2 of the response amplitude Q_{ana} as

$$Q_{ana} = \frac{\sqrt{Q_s^2 + Q_c^2}}{f_1}, \quad (\text{A8})$$

In order to evaluate the analytical expression for response amplitude, one can rewrite the Eq. (A4) as

$$x(t) = 1/\beta[-C_{0,\pm}^1(\alpha_1 + \sigma)\exp(\alpha_1 t) - C_{0,\pm}^2(\alpha_2 + \sigma)\exp(\alpha_2 t) + S\cos(\omega_1 t - \phi_1) + S'\cos(\omega_2 t - \phi_2) - E_1\sigma], \quad (\text{A9})$$

where

$$S^2 = (E_{13}^2 + E_{12}^2)(\omega_1^2 + \sigma^2) + f_1^2 + 2f_1\omega_1 E_{13} - 2f_1\sigma E_{12}, \quad (\text{A10})$$

$$S'^2 = (E_{23}^2 + E_{22}^2)(\omega_2^2 + \sigma^2) + f_2^2 + 2f_2\omega_2 E_{23} - 2f_2\sigma E_{22}, \quad (\text{A11})$$

$$\phi_1 = \tan^{-1} \frac{f_1 - E_{12}\sigma + E_{13}\omega_1}{E_{12}\omega_1 + E_{13}\sigma}, \quad (\text{A12})$$

$$\phi_2 = \tan^{-1} \frac{f_2 - E_{22}\sigma + E_{23}\omega_2}{E_{22}\omega_2 + E_{23}\sigma}. \quad (\text{A13})$$

By substituting Eq.(A9) in Eq. (A7) one can get

$$Q_s^{0,\pm} = \frac{2}{nT\beta} \int_0^{nT} [-C_{0,\pm}^1(\alpha_1 + \sigma)\exp(\alpha_1 t) - C_{0,\pm}^2(\alpha_2 + \sigma)\exp(\alpha_2 t) + S\cos(\omega_1 t - \phi_1) + S'\cos(\omega_2 t - \phi_2) - E_1\sigma] \sin(\omega_1 t) dt, \quad (\text{A14})$$

$$Q_c^{0,\pm} = \frac{2}{nT\beta} \int_0^{nT} [-C_{0,\pm}^1(\alpha_1 + \sigma)\exp(\alpha_1 t) - C_{0,\pm}^2(\alpha_2 + \sigma)\exp(\alpha_2 t) + S\cos(\omega_1 t - \phi_1) + S'\cos(\omega_2 t - \phi_2) - E_1\sigma] \cos(\omega_1 t) dt. \quad (\text{A15})$$

During the time interval nT , the value of $x(t)$ flips between various regions namely, D_0 , D_+ , and D_- , and the intrusion times of $x(t)$ in each of the regions are identified separately. Then the sine and cosine components of $x(t)$ in each of the components of sine ($Q_s^{0,\pm}$) and cosine ($Q_c^{0,\pm}$) are added successively depending on their dwelling in the three different regions D_0 , D_{\pm} . Finally the response amplitude Q is calculated as

$$Q_{ana} = \frac{\sqrt{(\sum Q_s^{0,\pm})^2 + (\sum Q_c^{0,\pm})^2}}{f_1}, \quad (\text{A16})$$

to obtain the analytical response amplitude.

- ¹P. Landa and P. V. McClintock, "Vibrational resonance," J. Phys. A Math. Gen. **33**, L433 (2000).
- ²S. Rajasekar and M. A. F. Sanjuan, *Nonlinear Resonances* (Springer, 2016).
- ³T. Roy-Layinde, J. Laoye, O. Popoola, U. E. Vincent, and P. V. E. McClintock, "Vibrational resonance in an inhomogeneous medium with periodic dissipation," Phys. Rev. E **96**, 032209 (2017).
- ⁴M. Ge, L. Lu, Y. Xu, R. Mamatimin, Q. Pei, and Y. Jia, "Vibrational mono-/bi-resonance and wave propagation in FitzHugh-Nagumo neural systems under electromagnetic induction," Chaos Soli. & Frac. **133**, 109645 (2020).
- ⁵T. Roy-Layinde, U. E. Vincent, S. Abolade, O. Popoola, J. Laoye, and P. V. McClintock, "Vibrational resonances in driven oscillators with position-dependent mass," Philos. Trans. R. Soc. A **379**, 20200227 (2021).
- ⁶P. Palaniyandi and M. Lakshmanan, "Estimation of system parameters and predicting the flow function from time series of continuous dynamical systems," Phys. Lett. A **338**, 253–260 (2005).
- ⁷J. Baltanás, L. Lopez, I. Blechman, P. Landa, A. Zaikin, J. Kurths, and M. Sanjuán, "Experimental evidence, numerics, and theory of vibrational resonance in bistable systems," Phys. Rev. E **67**, 066119 (2003).
- ⁸M. Bordet and S. Morfu, "Experimental and numerical enhancement of vibrational resonance in neural circuit," Electron. Lett. **48**, 903–905 (2012).
- ⁹M. Lakshmanan and S. Rajasekar, *Nonlinear Dynamics: Integrability, Chaos and Patterns* (Springer-Verlag Berlin Heidelberg, 2003).
- ¹⁰J. Yang and X. Liu, "Controlling vibrational resonance in a multistable system by time delay," Chaos **20**, 033124 (2010).
- ¹¹B. Deng, J. Wang, X. Wei, H. Yu, and H. Li, "Theoretical analysis of vibrational resonance in a neuron model near a bifurcation point," Phys. Rev. E **89**, 062916 (2014).

- ¹²L. Yang, W. Liu, M. Yi, C. Wang, Q. Zhu, X. Zhan, and Y. Jia, "Vibrational resonance induced by transition of phase-locking modes in excitable systems," *Phys. Rev. E* **86**, 016209 (2012).
- ¹³W. Guo and L. Ning, "Vibrational resonance in a fractional order quintic oscillator system with time delay feedback," *Int. J. Bifurc. Chaos* **30**, 2050025 (2020).
- ¹⁴B. Deng, J. Wang, and X. Wei, "Effect of chemical synapse on vibrational resonance in coupled neurons," *Chaos* **19**, 013117 (2009).
- ¹⁵B. Deng, J. Wang, X. Wei, K. Tsang, and W. L. Chan, "Vibrational resonance in neuron populations," *Chaos* **20**, 013113 (2010).
- ¹⁶C. Wang, K. Yang, and S. Qu, "Vibrational resonance in a discrete neuronal model with time delay," *Int. J. Mod. Phys. B* **28**, 1450103 (2014).
- ¹⁷P. Sarkar and D. S. Ray, "Vibrational antiresonance in nonlinear coupled systems," *Phys. Rev. E* **99**, 052221 (2019).
- ¹⁸L. Ning and Z. Chen, "Vibrational resonance analysis in a gene transcriptional regulatory system with two different forms of time-delays," *Phys. D: Nonlinear Phenom* **401**, 132164 (2020).
- ¹⁹P. Venkatesh and A. Venkatesan, "Vibrational resonance and implementation of dynamic logic gate in a piecewise-linear Murali-Lakshmanan-Chua circuit," *Commun. Nonlinear Sci. Numer. Simul.* **39**, 271–282 (2016).
- ²⁰R. Gui, Y. Wang, Y. Yao, and G. Cheng, "Enhanced logical vibrational resonance in a two-well potential system," *Chaos Solit. Fractals* **138**, 109952 (2020).
- ²¹K. Murali, S. Rajasekar, M. V. Aravind, V. Kohar, W. Ditto, and S. Sinha, "Construction of logic gates exploiting resonance phenomena in nonlinear systems," *Philos. Trans. R. Soc. A* **379**, 20200238 (2021).
- ²²L. Xiao, X. Zhang, S. Lu, T. Xia, and L. Xi, "A novel weak-fault detection technique for rolling element bearing based on vibrational resonance," *J. Sound Vib.* **438**, 490–505 (2019).
- ²³V. Chizhevsky and G. Giacomelli, "Vibrational resonance and the detection of aperiodic binary signals," *Phys. Rev. E* **77**, 051126 (2008).
- ²⁴P. Jia, C. Wu, J. Yang, M. A. Sanjuán, and G. Liu, "Improving the weak aperiodic signal by three kinds of vibrational resonance," *Nonlinear Dyn.* **91**, 2699–2713 (2018).
- ²⁵L. Xiao, J. Tang, X. Zhang, and T. Xia, "Weak fault detection in rotating machineries by using vibrational resonance and coupled varying-stable nonlinear systems," *J. Sound Vib.* **478**, 115355 (2020).
- ²⁶Y. Pan, F. Duan, F. Chapeau-Blondeau, L. Xu, and D. Abbott, "Study of vibrational resonance in nonlinear signal processing," *Philos. Trans. R. Soc. A* **379**, 20200235 (2021).
- ²⁷Y. Yang, J. Xu, Y. Kuang, H. Tu, H. Wei, H. Yang, K. Min, and W. Yang, "Research of weak signal detection based on super-regenerative chaotic oscillator," *Elec. Lett.* **58**, 194–196 (2022).
- ²⁸P. R. Venkatesh, A. Venkatesan, and M. Lakshmanan, "Implementation of dynamic dual input multiple output logic gate via resonance in globally coupled Duffing oscillators," *Chaos* **27**, 083106 (2017).
- ²⁹M. Sathish Aravindh, A. Venkatesan, and M. Lakshmanan, "Strange non-chaotic attractors for computation," *Phys. Rev. E* **97**, 052212 (2018).
- ³⁰Y. Yao and J. Ma, "Logical stochastic and vibrational resonances induced by periodic force in the FitzHugh-Nagumo neuron," *Eur. Phys. J. Plus* **137**, 1214 (2022).
- ³¹P. R. Venkatesh, A. Venkatesan, and M. Lakshmanan, "Design and implementation of dynamic logic gates and RS flip-flop using quasiperiodically driven Murali-Lakshmanan-Chua circuit," *Chaos* **27**, 033105 (2017).
- ³²M. Sathish Aravindh, R. Gopal, A. Venkatesan, and M. Lakshmanan, "Realisation of parallel logic elements and memory latch in a quasiperiodically-driven simple nonlinear circuit," *Pramana* **94** (2020)..
- ³³A. Chowdhury, M. G. Clerc, S. Barbay, I. Robert-Philip, and R. Braive, "Weak signal enhancement by nonlinear resonance control in a forced nano-electromechanical resonator," *Nat. Commun* **11**, 2400 (2020).
- ³⁴L. Xiao, R. Bajric, J. Zhao, J. Tang, and X. Zhang, "An adaptive vibrational resonance method based on cascaded varying stable-state nonlinear systems and its application in rotating machine fault detection," *Nonlinear Dyn.* **103**, 715–739 (2021).
- ³⁵Y. Ren, Y. Pan, F. Duan, F. Chapeau-Blondeau, and D. Abbott, "Exploiting vibrational resonance in weak-signal detection," *Phys. Rev. E* **96**, 022141 (2017).
- ³⁶Y. Ren, Y. Pan, and F. Duan, "Generalized energy detector for weak random signals via vibrational resonance," *Phys. Lett. A* **382**, 806–810 (2018).
- ³⁷K. Murali, M. Lakshmanan, and L. O. Chua, "The simplest dissipative nonautonomous chaotic circuit," *IEEE Trans. Circuits Syst. I. Fundam. Theory Appl.* **41**, 462–463 (1994).
- ³⁸U. ÇAM and R. Kiliç, "Inductorless realization of nonautonomous MLC chaotic circuit using current-feedback operational amplifiers," *J. Circuits Syst. Comput.* **14**, 99–107 (2005).
- ³⁹R. Kiliç, "Mixed-mode chaotic circuit with Wien-bridge configuration: The results of experimental verification," *Chaos Solit. Fractals* **32**, 1188–1193 (2007).
- ⁴⁰E. Günay, "MLC circuit in the frame of CNN," *Int. J. Bifurc. Chaos* **20**, 3267–3274 (2010).
- ⁴¹P. Swathy and K. Thamilaran, "Dynamics of SC-CNN based variant of MLC circuit: An experimental study," *Int. J. Bifurc. Chaos* **24**, 1430008 (2014).
- ⁴²E. Günay, K. Altun, and C. Ünal, "Implementation of CSK communicating system with switched SC-CNN based chaos generator," in *2017 10th International Conference on Electrical and Electronics Engineering (ELECO)* (IEEE) pp. 1364–1367.
- ⁴³P. Ashokkumar, M. Sathish Aravindh, A. Venkatesan, and M. Lakshmanan, "Realization of all logic gates and memory latch in the SC-CNN cell of the simple nonlinear MLC circuit," *Chaos* **31**, 063119 (2021).
- ⁴⁴T. F. Fozin, B. K. Nzoko, N. A. K. Telem, Z. T. Njitacke, A. A. N. Mouelas, and J. Kengne, "Coexistence of hyperchaos with chaos and its control in a diode-bridge memristor based MLC circuit with experimental validation," *Phys. Scr.* **97**, 075204 (2022).
- ⁴⁵L. O. Chua and L. Yang, "Cellular neural networks: Theory," *IEEE Transactions on circuits and systems* **35**, 1257–1272 (1988).
- ⁴⁶P. Arena, S. Baglio, L. Fortuna, and G. Manganaro, "Simplified scheme for realisation of Chua oscillator by using SC-CNN cells," *Electron. Lett.* **31**, 1794–1795 (1995).
- ⁴⁷P. Swathy and K. Thamilaran, "An experimental study on SC-CNN based canonical Chua's circuit," *Nonlinear Dyn.* **71**, 505–514 (2013).
- ⁴⁸T. Luo and Z. Wang, "Dynamics and SC-CNN circuit implementation of a periodically forced non-smooth mechanical system," *Nonlinear Dyn.* **85**, 23–45 (2016).
- ⁴⁹H. Li, J. Liu, and L. Du, "Vibrational resonance in the canonical Chua's circuit with a smooth nonlinear resistor," *Authorea Preprints* (2022).
- ⁵⁰G. Manganaro, P. Arena, and L. Fortuna, *Cellular neural networks: chaos, complexity and VLSI processing*, Vol. 1 (Springer Science & Business Media, 2012).
- ⁵¹M. Lakshmanan and K. Murali, *Chaos in Nonlinear Oscillators: Controlling and Synchronization*, Vol. 13 (World scientific, 1996).